Machine-learning accelerated density-explicit polymer field theory simulations

Duyu Chen,[1] Yao Xuan,[2] Hector D. Ceniceros,[2] and Glenn H. Fredrickson[1,3]

[1] *Materials Research Laboratory, University of California, Santa Barbara, California 93106, USA*

[2] *Department of Mathematics, University of California, Santa Barbara, California 93106, USA*

[3] *Department of Chemical Engineering, University of California, Santa Barbara, California 93106, United States*

(*Electronic mail: ghf@mrl.ucsb.edu)

(*Electronic mail: duyu@alumni.princeton.edu)

(Dated: 11 December 2025)

Recently, the density-explicit framework that describes thermodynamic properties of multicomponent polymer systems as functionals of both auxiliary and density fields has attracted growing interest in polymer field theory simulations. This is due to the flexibility of the framework in accommodating various forms of intermolecular potentials, and in particular, the easy generalization to many-body interactions beyond pair potentials. However, numerical simulations based on the formalism are generally more expensive owing to the increased number of fields, compared to the conventional auxiliary field framework. In this work, we develop deep neural networks with efficient low-dimensional and largely local feature representations that are applicable across different spatial resolutions and dimensions to accelerate polymer field theory simulations based on this framework. Our results may serve as a stepping stone toward accurate and efficient prediction of the phase behavior of complex block copolymer mesophases, as well as a blueprint for developing machine learning-assisted field theoretic simulation tools for the computational study of polymers and soft matter systems more broadly.

I. INTRODUCTION

Computer simulations[1–4] based on polymer field theory[5] have been widely used to investigate the equilibrium phase behavior of heterogeneous polymers during the last few decades. Depending on the amount of fluctuations included, field theory studies can be further divided into three categories: self-consistent field theory (SCFT) simulations that are at the mean-field level and incorporate no fluctuations, random-phase approximation (RPA) studies that involve Gaussian fluctuations around homogeneous mean-field solutions, and fully fluctuating field-theoretic simulations (FTS) that take into account all fluctuations.[2,6] Most previous field theory studies have adopted the standard auxiliary-field (AF) framework,[1,2] in which Hubbard–Stratonovich transformations[7] are utilized to decouple non-bonded interactions among polymer chains and replace them with independent interactions between a single polymer chain and one or more auxiliary potential fields $w(\mathbf{r})$.[2] The AF framework, despite its popular use, requires that the pair potential $u(r)$ is positive or negative definite and possesses an inverse, and is difficult to generalize to many-body interactions beyond pairwise interactions.[2,8–10]

Recently, efforts have been devoted to develop simulation tools based on the hybrid density-explicit auxiliary field (DE-AF) framework.[10] In this alternative framing of polymer field theory, both species density fields $\rho(\mathbf{r})$ and auxiliary potential fields $w(\mathbf{r})$ are retained.[11] In particular, in the inner loop, the auxiliary fields are sampled or relaxed toward a partial saddle point for given density fields, while in the outer loop, the density fields are sampled or relaxed toward the overall saddle point of the Hamiltonian. This setting removes the pair potential constraint on the interaction potentials in the AF framework. Also, in the DE-AF framework, one has access to physical observables associated with instantaneous density fields, which enables the analysis of experimentally obtained density profiles and simulations of non-equilibrium systems, e.g., in the context of dynamic self-consistent field theory (DSCFT).[11–16] It is worth noting that in a DSCFT simulation, the outer loop evolves the density fields according to prescribed dynamics, whereas the inner loop is equivalent to that in a density-explicit FTS simulation. Consequently, simulation tools developed for FTS can also be directly applied to, or adapted for, DSCFT calculations. However, both density-explicit FTS and DSCFT simulations remain computationally demanding,[10] as the inner loop iteration must be performed repeatedly–once for every outer-loop update of the density fields. Because typical simulations involve tens of thousands or more outer-loop iterations, the acceleration of the inner loop solver is crucial for improving overall computational efficiency.

The rapid development of machine learning (ML) tools, in particular those based on deep neural networks in recent years presents transformative opportunities to enhance and accelerate polymer field theory, enabling novel phase discovery and the prediction of self-assembly behavior in block copolymer systems with unprecedented efficiency.[17–24] For example, Xuan et al.[17,18] trained ML models to predict the effective Hamiltonian and saddle points of the density fields obtained from SCFT simulations in the AF framework, which accelerates the computational exploration of design parameter space for block copolymers. Chen and Dorfman[19] leveraged a deep convolutional generative adversarial network to propose new initial fields for SCFT calculations that enable de novo phase discovery. Nakamura[20] developed a neural network model with a theory-embedded layer to predict the phase behavior of polymeric solutions. Various neural network-based solvers[21,22] have also been developed to tackle the partial differential equations in SCFT. Yong and Kim[24] trained a deep neural network to predict the difference between trial and partial saddle points of the pressure field from a given exchange field in the AF framework, enabling accelerated FTS simulations (note that here, partial saddle points are defined with respect to the pressure field, rather than all of the auxiliary fields in the density-explicit framework).

In this work, we leverage deep neural networks to accelerate simulations based on the DE-AF field theory framework, using the incompressible melt of a linear AB diblock copolymer with the continuous Gaussian chain model as an example. We first investigate partial saddle point solutions of the auxiliary fields for various representative density fields, both analytically and numerically. Insights from this analysis guide the design of neural networks with efficient low-dimensional and largely local feature representations. These neural networks are trained on one-dimensional simulation data to predict partial saddle points, which are then used to initialize new FTS simulations. Interestingly, our ML models accelerate large-cell simulations with high spatial resolution, even though they are trained on data obtained at much lower resolution. Furthermore, after fine-tuning the model with a small amount of three-dimensional data from perturbed body-centered-cubic (BCC) sphere phases, it achieves high prediction accuracy and speeds up simulations in three dimensions. Our ML models and results could serve as blueprints for the accelerated computational prediction of the self-assembly behavior of heterogeneous polymers.

II. THEORETICAL AND SIMULATION METHODS

Here, we introduce the specific model and assumptions that are used in the polymer field theory simulations in this study. In the DE-AF framework, the canonical partition function $Z_C(n,V,T)$ for the incompressible melt of a linear AB diblock copolymer with the continuous Gaussian chain model is given by[10]

$$Z_C(n,V,T) = Z_0 \int D\phi \int Dw_A \int Dw_B \, e^{-H[\phi,w_A,w_B]}, \tag{1}$$

$$\begin{aligned} H[\phi,w_A,w_B] = C\Bigg\{ &\chi N \int d\mathbf{r}\,\phi(\mathbf{r})[1-\phi(\mathbf{r})] - \int d\mathbf{r}\, iw_A(\mathbf{r})\phi(\mathbf{r}) \\ &- \int d\mathbf{r}\, iw_B(\mathbf{r})[1-\phi(\mathbf{r})] - \bar{V}\ln Q[iw_A,iw_B] \Bigg\}, \end{aligned} \tag{2}$$

where Z_0 is the ideal gas contribution, n is the number of polymers, V is the volume, N is the polymer degree of polymerization, and $\rho_0 = nN/V$ is the average polymer segment density. Parameters in the model include the Flory–Huggins interaction parameter χ, the volume fraction of type A segments $f = N_A/(N_A+N_B)$, the dimensionless chain concentration $C = nR_g^3/V$, the dimensionless volume $\bar{V} = V/R_g^3$, and the unperturbed polymer radius of gyration R_g (all lengths in the model are scaled by R_g). The field $\phi(\mathbf{r}) = \phi_A(\mathbf{r}) = \rho_A(\mathbf{r})/\rho_0$ is the species volume fraction or normalized density field of the A block, and $w_A(\mathbf{r})$ and $w_B(\mathbf{r})$ are the species auxiliary fields (normalized by N) of the A and B blocks, respectively. Note that due to the incompressible melt condition, the volume fraction field $\phi_B(\mathbf{r})$ of the B block is given by $\phi_B(\mathbf{r}) = 1-\phi(\mathbf{r})$. Here, the normalized partition function $Q[iw_A,iw_B]$ is given by

$$Q[iw_A,iw_B] = \frac{1}{\bar{V}}\int d\mathbf{r}\, q(\mathbf{r},1;[iw_A,iw_B]) = \frac{1}{\bar{V}}\int d\mathbf{r}\, q_c(\mathbf{r},1;[iw_A,iw_B]), \tag{3}$$

where the chain propagator $q(\mathbf{r},s;[iw_A,iw_B])$ satisfies the Fokker-Planck equation

$$\frac{\partial}{\partial s} q(\mathbf{r},s;[iw_A,iw_B]) = \nabla^2 q(\mathbf{r},s;[iw_A,iw_B]) - iw(\mathbf{r},s)q(\mathbf{r},s;[iw_A,iw_B]), \tag{4}$$

and is initialized from the A block end with the initial condition $q(\mathbf{r},0)=1$, and the corresponding auxiliary field $w(\mathbf{r},s)$ is given by

$$w(\mathbf{r},s) = \begin{cases} w_A(\mathbf{r}), & 0 \le s \le f, \\ w_B(\mathbf{r}), & f < s \le 1. \end{cases} \tag{5}$$

The complementary chain propagator $q_c(\mathbf{r},s;[iw_A,iw_B])$, on the other hand, propagates from the B block end with the initial condition $q_c(\mathbf{r},0)=1$, and satisfies the analogous diffusion equation

$$\frac{\partial}{\partial s}q_c(\mathbf{r},s;[iw_A,iw_B]) = \nabla^2 q_c(\mathbf{r},s;[iw_A,iw_B]) - iw_c(\mathbf{r},s)q_c(\mathbf{r},s;[iw_A,iw_B]), \tag{6}$$

where the corresponding auxiliary field $w_c(\mathbf{r},s)$ is given by

$$w_c(\mathbf{r},s) = \begin{cases} w_B(\mathbf{r}), & 0 \le s \le 1-f, \\ w_A(\mathbf{r}), & 1-f < s \le 1. \end{cases} \tag{7}$$

Note that here we define the complementary propagator $q_c(\mathbf{r},s)$ as a propagator starting from the B-block end at $s=0$. This differs from the reverse propagator $q^\dagger(\mathbf{r},s)$ used in some other SCFT works,[4,25] which propagates backward from the B-block end at $s=1$. These are equivalent representations related by $q^\dagger(\mathbf{r},s) = q_c(\mathbf{r},1-s)$.

To evaluate the functional integrals with respect to the auxiliary fields $w_A(\mathbf{r})$ and $w_B(\mathbf{r})$ in the partition function, one can further invoke the partial saddle-point approximation (PSPA),[10] and replace the integrals with the leading (mean-field) contribution, i.e.,

$$\int Dw_A \int Dw_B e^{-H[\phi,w_A,w_B]} \approx e^{-H[\phi,w_A^*[\phi],w_B^*[\phi]]}, \tag{8}$$

$$\left.\frac{\delta H[\phi,w_A,w_B]}{\delta w_A(\mathbf{r})}\right|_{w_A^*[\phi],w_B^*[\phi]} = -iC\left\{\phi(\mathbf{r}) - \tilde{\phi}_A(\mathbf{r})\right\} = 0, \tag{9}$$

$$\left.\frac{\delta H[\phi,w_A,w_B]}{\delta w_B(\mathbf{r})}\right|_{w_A^*[\phi],w_B^*[\phi]} = -iC\left\{1-\phi(\mathbf{r}) - \tilde{\phi}_B(\mathbf{r})\right\} = 0. \tag{10}$$

where the volume fraction operators $\tilde{\phi}_A(\mathbf{r})$ and $\tilde{\phi}_B(\mathbf{r})$ are given by

$$\tilde{\phi}_A(\mathbf{r}) = -\bar{V}\frac{\delta \ln Q}{\delta iw_A} = \frac{1}{Q[iw_A,iw_B]}\int_0^f ds\, q_c(\mathbf{r},1-s;[iw_A,iw_B])q(\mathbf{r},s;[iw_A,iw_B]), \tag{11}$$

and

$$\tilde{\phi}_B(\mathbf{r}) = -\bar{V}\frac{\delta \ln Q}{\delta iw_B} = \frac{1}{Q[iw_A,iw_B]}\int_f^1 ds\, q_c(\mathbf{r},1-s;[iw_A,iw_B])q(\mathbf{r},s;[iw_A,iw_B]). \tag{12}$$

We note that while in the auxiliary field framework the w fields often have many saddle points, each corresponding to a unique density profile, in the density-explicit framework the partial saddle point of the auxiliary fields for a given density field $\phi(\mathbf{r})$ is generally unique (up to constants). Moreover, these equations governing the partial saddle point reveal that the mapping from $\phi(\mathbf{r})$ to $w_A(\mathbf{r})$ and $w_B(\mathbf{r})$ is inherently nonlinear and nonlocal for general density profiles $\phi(\mathbf{r})$.

Alternatively, one can also utilize complex Langevin (CL) dynamics[10] to sample the field states representative of the complex distribution $\exp(-H[\phi, w_A, w_B])$, which is a more accurate but also more computationally intensive way to evaluate the integrals with respect to $w_A(\mathbf{r})$ and $w_B(\mathbf{r})$. It is noteworthy that even with the PSPA, approximating these integrals is computationally expensive, given the cost to find the partial saddle points $w_A^*[\phi]$ and $w_B^*[\phi]$ in particular for instantaneous density fields $\phi(\mathbf{r})$ that are not saddle points of H. In this work we focus on FTS simulations based on PSPA.

III. PARTIAL SADDLE POINTS OF INSTANTANEOUS DENSITY FIELDS

Here, we analytically and numerically investigate the factors influencing the solutions of partial saddle points of the auxiliary fields across different density profiles. We consider both saddle-point and non-saddle-point configurations, which allows for a more complete understanding of the system and helps identify the features that machine learning models should take into account when predicting partial saddle points.

A. Saddle-point density fields

In the DE-AF framework, when the instantaneous density fields are also saddle points $\phi^*(\mathbf{r})$ of the density fields, i.e.,

$$\left.\frac{\delta H[\phi, w_A, w_B]}{\delta \phi(\mathbf{r})}\right|_{\phi^*} = 0, \tag{13}$$

the partial saddle points $w_A^*[\phi]$ and $w_B^*[\phi]$ are saddle points of the Hamiltonian $H[\phi, w_A, w_B]$ for a simulation box with a *fixed* shape and volume, i.e., they coincide with SCFT solutions. Plugging Eq. 2 into Eq. 13, one arrives at the following relationship:

$$i[w_A^*(\mathbf{r}) - w_B^*(\mathbf{r})] = \chi N[1 - 2\phi^*(\mathbf{r})]. \tag{14}$$

Interestingly, this is a *local linear* relationship, i.e., the difference $w_A^* - w_B^*$ in the auxiliary fields at a given spatial grid point $\mathbf{r}$ is only related to the density field ϕ at that spatial grid point. We note that Eq. 13 is analogous to the SCFT saddle point condition in the AF framework,[26] except that here the auxiliary fields $w_A^*(\mathbf{r})$ and $w_B^*(\mathbf{r})$ are purely imaginary while the corresponding saddle point auxiliary fields in the AF framework can be either real or pure imaginary depending on the sign of the eigenvalue of the exchange normal mode. Recently, it has been found that SCFT equations in the AF framework admit additional complex-valued saddle points,[26] but here we focus on physically meaningful solutions – restricting attention to saddle points with real-valued density fields and purely imaginary $w_A^*(\mathbf{r})$ and $w_B^*(\mathbf{r})$. In addition, if $w_A^*[\phi]$ and $w_B^*[\phi]$ are partial saddle points for a given $\phi(\mathbf{r})$, then adding a constant to either $w_A^*[\phi]$ or $w_B^*[\phi]$ preserves the partial saddle point condition. This implies a nonuniqueness in the solutions for $w_A^*[\phi]$ or $w_B^*[\phi]$. In this work, to eliminate this trivial degeneracy, we set

$$\int d\mathbf{r}\, w_A^*(\mathbf{r}) = \int d\mathbf{r}\, w_B^*(\mathbf{r}) = 0. \tag{15}$$

Under this normalization, we have

$$i[w_A^*(\mathbf{r}) - w_B^*(\mathbf{r})] = 2\chi N[f - \phi^*(\mathbf{r})], \tag{16}$$

where f is the spatially averaged volume fraction of the A block.

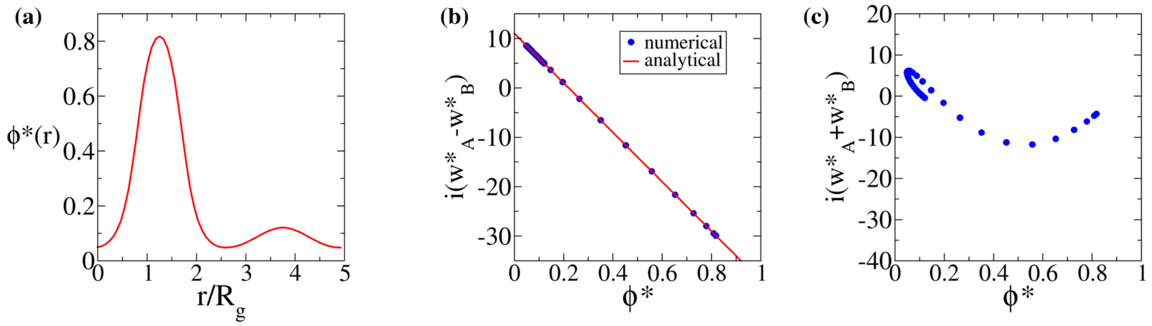

FIG. 1. The saddle point density profile $\phi^*(\mathbf{r})$ (a) solved by the auxiliary field SCFT simulation at $\chi N = 25$, $f = 0.22$ and $L = 5.0R_g$, and the corresponding converged $w_A^*[\phi^*] - w_B^*[\phi^*]$ (b) and $w_A^*[\phi^*] + w_B^*[\phi^*]$ (c) fields in the DE-AF simulation. The analytical expression given in Eq. 16 that links $w_A^*[\phi^*] - w_B^*[\phi^*]$ to $\phi^*(\mathbf{r})$ is shown in (b) to compare to simulation.

As a representative example, we ran one-dimensional auxiliary-field SCFT simulations at $\chi N = 25$, $f = 0.22$ and box length $L = 5.0R_g$. The simulations were subject to periodic boundary conditions and the converged saddle point field $\phi^*(\mathbf{r})$ is shown in Fig. 1(a), which is a (defective) layered structure with a large primary peak and a small secondary peak in the real-space density profile. Subsequently, we use this converged $\phi^*(\mathbf{r})$ as the target density profile in the DE-AF framework and numerically obtain the corresponding $w_A^*[\phi^*]$ and $w_B^*[\phi^*]$. Indeed, Fig. 1(b) shows $iw_A^* - iw_B^*$

against the values of ϕ^*, exhibiting quantitative agreement with the analytical expression given in Eq. 16, provided that the difference between consecutive field iterates (i.e., field error tolerance) is set to 10^{-8}. In contrast, a field error tolerance of 10^{-5} is deemed sufficient for the thermodynamic properties of interest. For instance, this level of tolerance yields an error in the Hamiltonian of order $10^{-7} k_B T$ per chain in the DE-AF simulation. On the other hand, the dependence of $iw_A^* + iw_B^*$ on $\phi^*(\mathbf{r})$ is highly nonlocal and nonlinear, and can involve a multi-valued mapping, i.e., a given value of ϕ^* could correspond to multiple values of $iw_A^* + iw_B^*$, as shown in Fig. 1(c). This relationship is strongly influenced by the specific shape of $\phi^*(\mathbf{r})$. We note that in these scatter plots, each point represents a scalar pair $(\phi, w^*[\phi])$, leading to 64 such pairs (some points are overlapping) for a density field with a spatial resolution of 64. Adjacency of points in the scatter plots does not necessarily imply spatial proximity.

B. Non-saddle point density fields

For density fields $\phi(\mathbf{r})$ that are not saddle points of H, Eq. 16 no longer holds, and the $w_A^*[\phi](\mathbf{r})$ and $w_B^*[\phi](\mathbf{r})$ fields are related to $\phi(\mathbf{r})$ in a nonlinear, nonlocal way as mentioned above. Here, we investigate numerically the relationships in these cases of non-saddle point $\phi(\mathbf{r})$. In particular, we consider non-saddle point $\phi(\mathbf{r})$ generated by a type of single-mode reciprocal-space perturbation. We start from a saddle-point $\phi^*(\mathbf{r})$, and generate a non-saddle point $\phi(\mathbf{r})$ by randomly varying the values of the Fourier transform $\hat{\phi}^*(\mathbf{q})$ of $\phi^*(\mathbf{r})$ for wave vectors $\mathbf{q}$ in a shell around the location $\mathbf{q}^*$ of the principal wave vector with a thickness δ, i.e.,

$$\hat{\phi}(\mathbf{q}) = \gamma \hat{\phi}^*(\mathbf{q}) \quad \text{for } ||\mathbf{q}| - |\mathbf{q}^*|| < \delta. \tag{17}$$

To make sure that $\phi(\mathbf{r})$ is real-valued, we set γ to be the same for any pair of $\mathbf{q}$ and $-\mathbf{q}$ that satisfy the above equation. For 1D small-cell simulations, we choose a sufficiently small δ such that the density profile is perturbed only at a single pair of $\mathbf{q}$ and $-\mathbf{q}$. To ensure that $\phi(\mathbf{r})$ is between 0 and 1 at each spatial grid point (so that it is physical and consistent with the incompressible melt condition), we sample the random coefficient γ from a uniform distribution in the range of [0.90, 1.0], i.e., $\gamma \sim U[0.90, 1.0]$. We choose γ values close to 1 since we intend to focus on structures that are well microphase-separated, and also avoid cases where the simulations either fail to find numerical solutions for the partial saddle points or converge very slowly. This also mimics a typical DE-AF simulation where the density fields are iteratively updated and, at each step, the auxiliary fields are relaxed to their partial saddle point corresponding to the newly updated density fields.

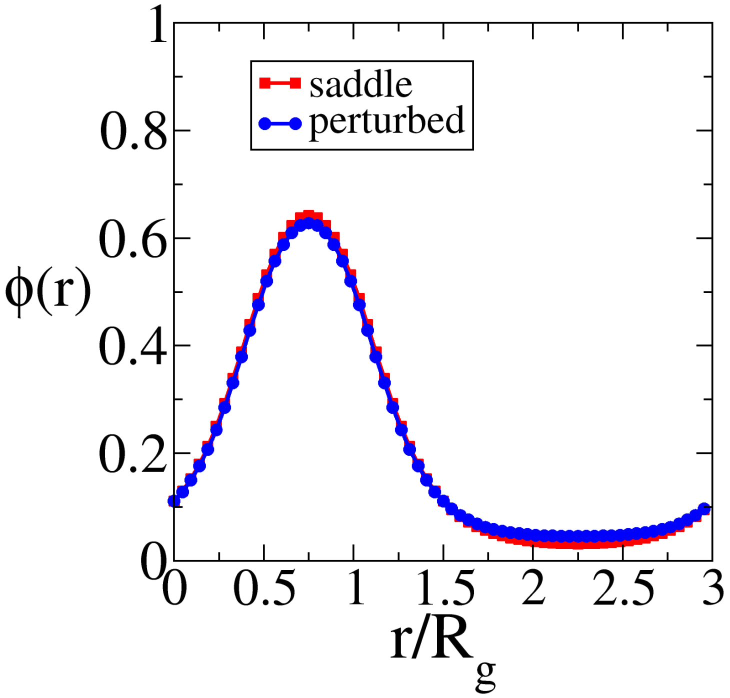

FIG. 2. A representative example of a non-saddle point $\phi(\mathbf{r})$ obtained by single-mode reciprocal-space perturbation of a saddle point at $\chi N = 25$, $f = 0.22$ and $L = 3.0R_g$.

Figure 2 shows an example of a non-saddle point $\phi(\mathbf{r})$ at $\chi N = 25$, $f = 0.22$ and $L = 3.0R_g$ obtained by this type of perturbation of the corresponding saddle point. This example illustrates that the specific type of perturbation that we consider essentially drives the system towards a more homogeneous state with slightly damped peak and valley in 1D. In Fig. 3 we present the numerically solved partial saddle points $w_A^*[\phi] - w_B^*[\phi]$ and $w_A^*[\phi] + w_B^*[\phi]$. The $w_A^* - w_B^*$ difference field is no longer a linear functional of $\phi(\mathbf{r})$; in particular, the nonlinearity is evident deep inside the B-rich region ($\phi \approx 0$).

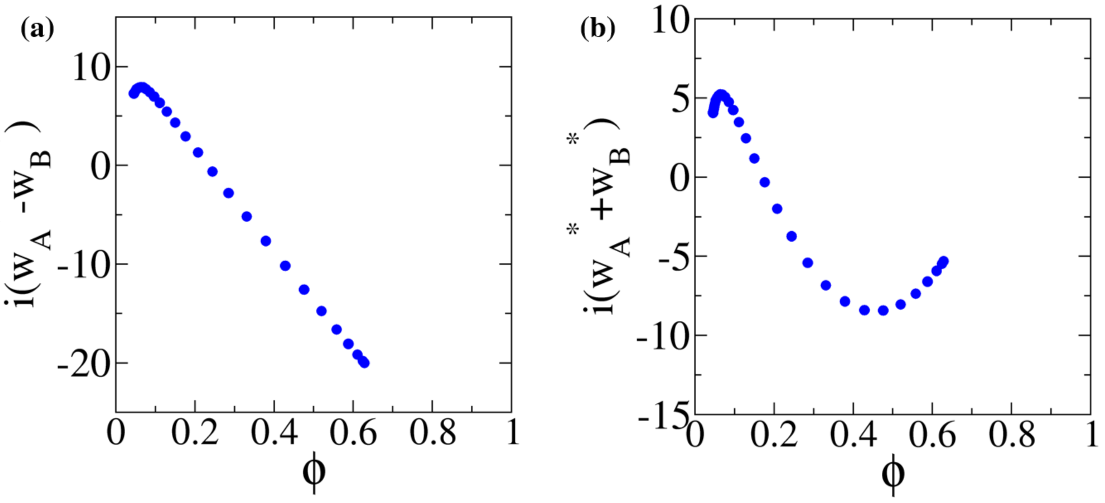

FIG. 3. Partial saddle points $w_A^*[\phi] - w_B^*[\phi]$ and $w_A^*[\phi] + w_B^*[\phi]$ for the non-saddle point $\phi(\mathbf{r})$ at $\chi N = 25$, $f = 0.22$ and $L = 3.0R_g$ in Fig. 2 from simulation.

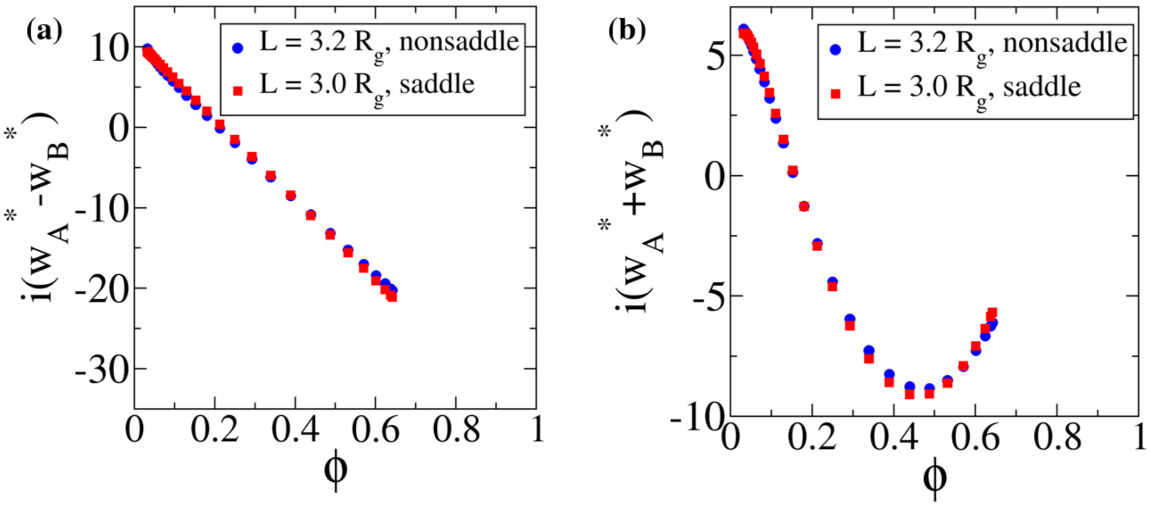

FIG. 4. Partial saddle points $w_A^*[\phi] - w_B^*[\phi]$ and $w_A^*[\phi] + w_B^*[\phi]$ for the non-saddle point $\phi(\mathbf{r})$ obtained by stretching the box of a saddle point $\phi(\mathbf{r})$ from $L = 3.0R_g$ to 3.2 R_g at $\chi N = 25$, $f = 0.22$, along with the partial saddle points at $L = 3.0R_g$.

C. Effect of domain spacing

To model an infinite or very large system in the bulk using a finite-size simulation box, computer simulations typically rely on periodic boundary conditions. System size and (in 2D or 3D) shape effects are particularly important in SCFT simulations of copolymer mesophases, which respond elastically as they are distorted away from their preferred equilibrium pattern.[2] The implication is that a saddle point configuration $\phi^*(\mathbf{r})$ at a given cell shape and volume will no longer be the saddle-point solution at another cell shape and volume. Specifically, in one dimension, the domain length of the box affects the partial saddle points w_A^* and w_B^*. As shown in Fig. 4, as one increases the box length L from 3.0 R_g to 3.2 R_g at $\chi N = 25$ and $f = 0.22$ (i.e., stretches the distance between adjacent grid points without changing the magnitudes of ϕ at each grid point), the saddle point $\phi^*(\mathbf{r})$ at $L = 3.0R_g$ is no longer a saddle point at $L = 3.2R_g$, and the solution of $iw_A^* - iw_B^*$ deviates slightly from the analytical form given by Eq. 16. Here we apply a small variation of L to avoid situations where the simulations fail to find numerical solutions for partial saddle points or converge very slowly.

IV. ML MODEL

Utilizing the insights obtained from analyzing the solutions of partial saddle points, we now design and train neural networks to accelerate DE-AF field-theoretic simulations under the PSPA assumption. We describe in this section the feature selection, model architecture, and data collection process for our ML model.

A. Local representation and model architecture

Recently, neural networks using local frame descriptors as features[27,28]—which describe the local environments around atoms—have been very successful in advancing deep potential molecular dynamics. Here, we follow a similar path and use a local density representation for our ML model in the context of field-based simulations. Specifically, we learn a local mapping from the local *scalar* ϕ, the magnitude of its gradient $|\nabla\phi|$ and its Laplacian $\nabla^2\phi$ at a given spatial grid point (and other global features) to the scalar values of w_A and w_B at that grid point. The inclusion of $\nabla^2\phi$ is motivated by the appearance of $\nabla^2 q$ in the governing equation for the chain propagator $q(\mathbf{r}, s; [iw_A, iw_B])$, which is connected to the volume fraction operator $\tilde{\phi}_A(\mathbf{r})$. This operator is constrained to match $\phi(\mathbf{r})$ under the partial saddle point condition. Regarding global features, it is well known that for conformationally symmetric AB linear diblock copolymers, the equilibrium phase behavior at the mean-field level is dictated by the volume fraction f of the A block and segregation strength χN at the mean field level.[2] Therefore, we incorporate χN and f as input features. Additionally, we incorporate ϕ_{max} and ϕ_{min}, representing the maximum and minimum values of the density profile, respectively. These features provide the model with global context about the profile, compensating for the fact that predictions are made independently at each spatial grid point. Furthermore, we select the principal wavenumber q^*—the wavenumber at which the structure factor $S(k)$ reaches its maximum—as a feature to encode information about the natural scale of the self-assembly, which is related to the cell shape and volume in the case of small-cell simulations.

This local mapping offers several advantages: it is independent of the specific copolymer mesophase, applicable across different spatial dimensions and resolutions, and invariant under translations and rotations of polymer species density fields. Moreover, generating the data required to learn this mapping is much less costly than learning a full mapping from a given *scalar field* $\phi(\mathbf{r})$ to the $w_A(\mathbf{r})$ and $w_B(\mathbf{r})$ fields in a simulation box with a given shape and volume. For instance, a single simulation of a 1D phase with a spatial resolution of 64 produces 64 samples under this local density representation, whereas it yields only one sample for a full mapping. Also, due to the low-dimensional nature of the feature space, training a ML model is much easier compared to using a feature representation based on the scalar field $\phi(\mathbf{r})$.

Given the complex nature of the mapping between the input features and the $w_A(\mathbf{r})$ and $w_B(\mathbf{r})$ fields, here we employ a feedforward deep neural network with fully connected layers to learn this mapping. We treat the number of hidden layers (i.e., depth of the neural network) and the number of neurons in each hidden layer (i.e., width of the neural network) as hyperparameters to tune. Considering the analytical relationship given by Eq. 16 for the saddle-point density $\phi(\mathbf{r})$, the neural network is trained to learn $u_- = i[w_A^*(\mathbf{r}) - w_B^*(\mathbf{r})] - 2\chi N[f - \phi(\mathbf{r})]$ and $u_+ = i[w_A^*(\mathbf{r}) + w_B^*(\mathbf{r})]$. The form of u_- is related to the saddle-point condition in Eq. 16 corresponds to the residual terms in the fields $w_A(\mathbf{r})$ and $w_B(\mathbf{r})$ fields and is reminiscent of the approach used in another recent ML study.[17] We use the mean squared error between the predicted values u_+ and u_- and their corresponding ground truth values $\tilde{u}+$ and $\tilde{u}-$ (obtained from DE-AF SCFT simulations) as the loss function $\mathscr{L}$.

Specifically,

$$\mathscr{L} = \frac{1}{2N_s}[\sum_{j=1}^{N_s}(u_{j,-} - \tilde{u}_{j,-})^2 + \sum_{j=1}^{N_s}(u_{j,+} - \tilde{u}_{j,+})^2], \tag{18}$$

where the index j runs over all samples, and N_s denotes the total number of samples. The Continuously Differentiable Exponential Linear Unit (CELU)[29] is used as the nonlinear activation function for all hidden layers, which produces the following output $\sigma(z)$ for a given input z:

$$\sigma(z) = \begin{cases} z, & z \geq 0, \\ \alpha[\exp(z/\alpha) - 1], & z < 0. \end{cases} \tag{19}$$

Here, we set the parameter $\alpha = 1$ for all hidden units. We find that CELU outperforms the widely used Rectified Linear Unit (ReLU) in our task, likely due to CELU's smooth gradients and ability to mitigate neuron inactivity. The model architecture of our neural network is schematically shown in Fig. 5.

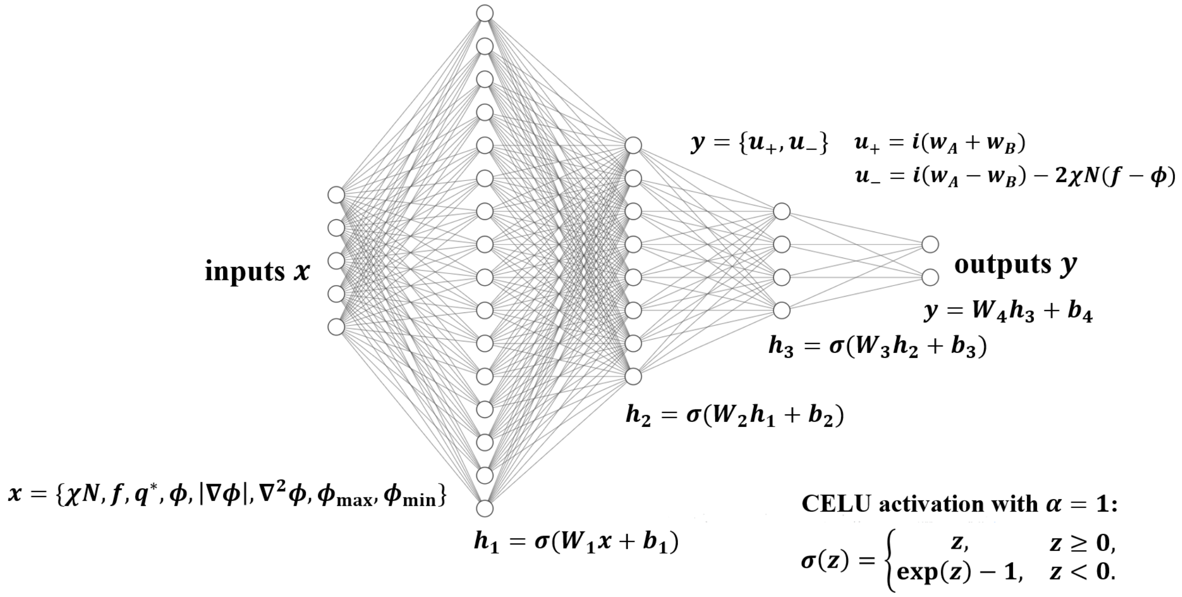

FIG. 5. Illustration of the model architecture for our deep neural networks with an efficient local density feature representation $(\chi N, f, q^*, \phi, |\nabla\phi|, \nabla^2\phi, \phi_{\max}, \phi_{\min})$.

B. Data collection

To generate the data for training and evaluating the neural network, we performed SCFT simulations with a fixed simulation box to obtain 1D saddle point density profiles for 160 microstructures with a spatial resolution of 64, covering the parameter ranges $\chi N \in \{25, 30, 35, 40\}$, $f \in \{0.22, 0.26, 0.30, 0.34, 0.38, 0.42, 0.46, 0.50\}$, and $L/R_g \in \{3.0, 3.5, 4.0, 4.5, 5.0\}$. We use these small-cell simulations to better resolve the structures at a given spatial resolution of 64. To incorporate non-saddle point cases into our dataset, we apply the previously described single-mode reciprocal-space perturbation to each saddle point density profile, generating 8 independent non-saddle point profiles per saddle point. To further displace the profiles from the saddle point, we also perturb the parameters χN and L according to $(\chi N)' = \gamma_1 \chi N$ and $L' = \gamma_2 L$ for these non-saddle points, where $\gamma_1 \sim U[0.95, 1.05]$ and $\gamma_2 \sim U[0.95, 1.05]$. Here we choose small perturbations for χN and L to avoid situations where the simulations fail to find numerical solutions for partial saddle points or converge very slowly. In total, we have collected 160+160×8=1440 density profiles with a spatial resolution of 64, which correspond to 1440×64=92160 samples due to the local density representation we are using. We set the field error tolerance to 10^{-8} for all simulations when generating the data set to ensure high data quality.

Subsequently, following standard practice, we randomly partition the collected data into three sets: a training set consisting of 1008 density profiles (or 64512 samples), a cross validation set consisting of 216 density profiles (or 13824 samples), and a test set consisting of 216 density profiles (or 13824 samples). The training set is used to learn the neural network parameters (weights and biases), the cross-validation set is used to tune hyperparameters, and the test set is used to assess the performance of the trained network on previously unseen data.

V. DATA-DRIVEN PREDICTION FOR PARTIAL SADDLE POINTS

A. ML model performance

We employ the Adaptive Moment Estimation (i.e., Adam) Optimizer[30] to train the aforementioned neural networks shown in Fig. 5 using the training set. The learning rate and weight decay of the Adam optimizer, along with the number of hidden layers and neurons per layer in the neural network, are treated as hyperparameters and tuned using the cross-validation set. Initially, we employed a simpler ML model using $(\chi N, f, q^*, \phi, |\nabla \phi|)$ as input features, but found that these

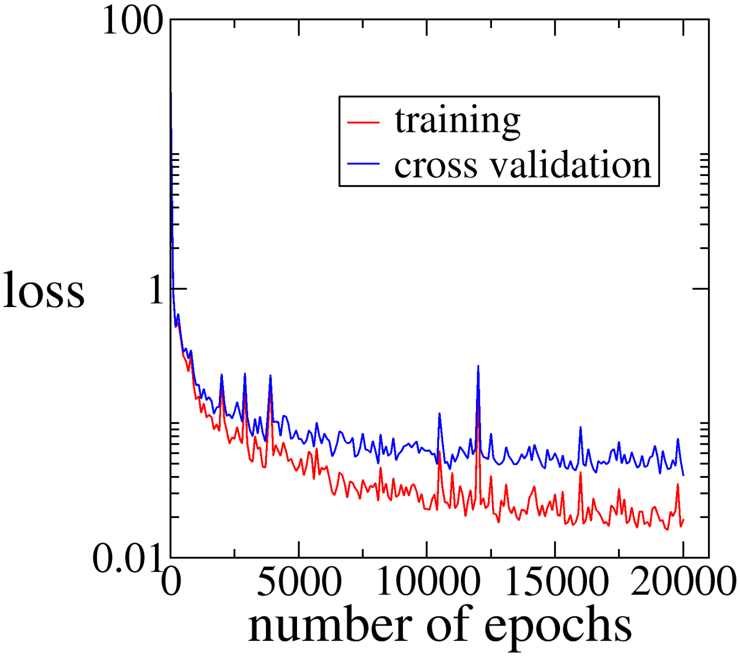

FIG. 6. Training and cross validation loss as functions of the number of epochs for the optimized neural network with three hidden layers containing 80, 40, and 16 neurons, respectively, trained using a batch size of 128, a learning rate of 5.0×10^{-4} and a weight decay of 1.0×10^{-5}.

features alone do not provide sufficient information to accurately predict partial saddle points (For this simpler model, the validation loss was as high as 2.8 after training). As a result, we incorporated the previously mentioned features $\nabla^2\phi, \phi_{\max}, \phi_{\min}$ into the feature set. The neural network was trained for 20000 epochs with a batch size of 128, and the best model was recorded that yields the lowest loss on the cross validation set after the first 10000 epochs. We were able to achieve a cross-validation loss $\mathscr{L}$ as low as 0.04 using a neural network with three hidden layers containing 80, 40, and 16 neurons, respectively, and a learning rate of 5.0×10^{-4} and a weight decay of 1.0×10^{-5}, as shown by the learning curves in Fig. 6. This performance underscores the value of including $\nabla^2\phi$, $\phi_{\max}$, and $\phi_{\min}$ as input features, which enrich the model with both local and global information about the density field and make up for the fact that we are using ML models that decouple different spatial grid points when making the predictions.

The performance of the trained ML model was evaluated by making predictions on the test

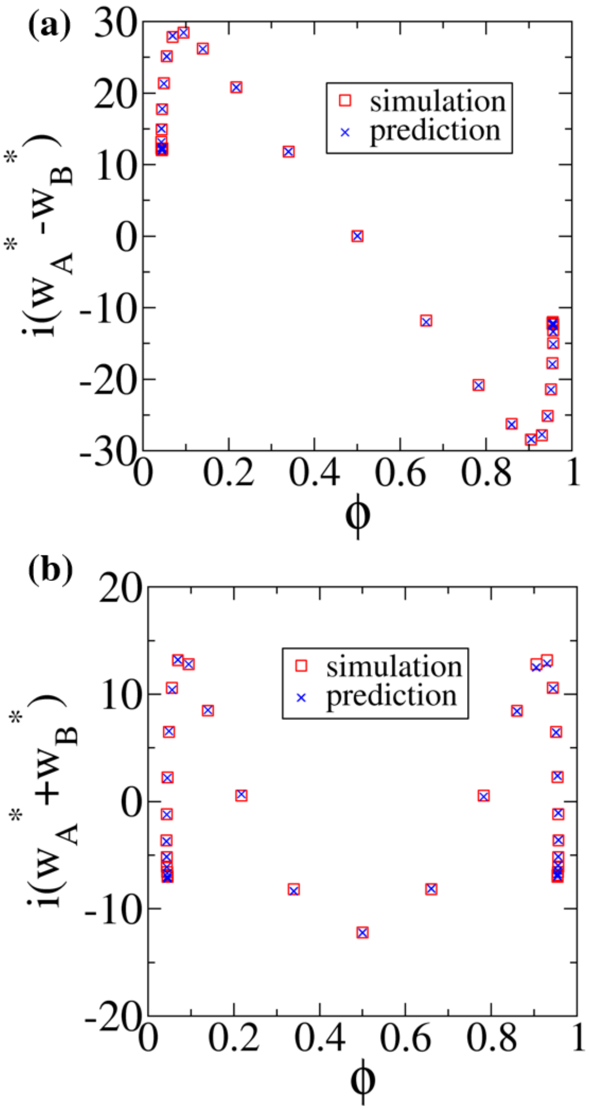

FIG. 7. Partial saddle points of $w_A^*[\phi]-w_B^*[\phi]$ (a) and $w_A^*[\phi]+w_B^*[\phi]$ (b) predicted by ML model (blue) and from DE-AF field theory simulation (red) for a non-saddle point density profile at $\chi N = 34.69$, $f = 0.50$, and $L = 4.98R_g$.

set that was never seen by the model during training or hyperparameter tuning. The loss $\mathscr{L}$ was found to be 0.03 for the test set, indicating that our model generalizes well to new, unseen data. As an example, we show in Fig. 7 the predicted and true partial saddle point of $w_A^*[\phi]-w_B^*[\phi]$ and $w_A^*[\phi]+w_B^*[\phi]$ for a non-saddle point density profile at $\chi N = 34.69$, $f = 0.50$, and $L = 4.98R_g$, which indicates excellent agreement between ML model prediction and simulation (see Sec. S1 of the supplementary material for more examples).

B. Acceleration of density-explicit simulations at high spatial resolution

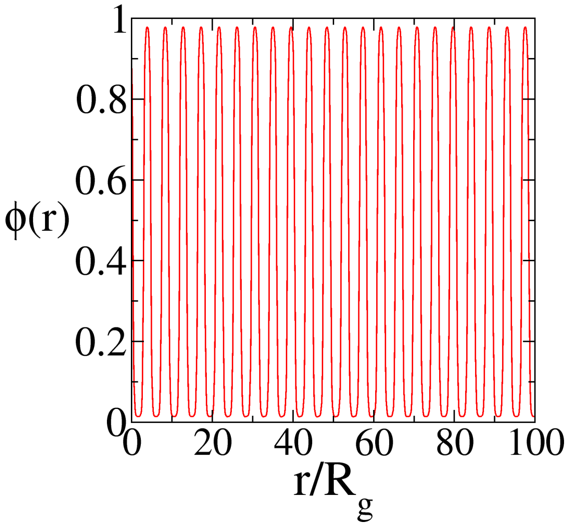

FIG. 8. Visualization of a non-saddle point density profile in a large cell with a high spatial resolution of 2048 at $\chi N = 30$, $f = 0.40$, and $205.19 R_g$. Here we only show a portion of the boxes for better visual clarity.

All the density profiles in the training, cross validation, and test set employed were 1D profiles with a spatial resolution of 64. However, due to the fact that the local density representation in the ML model decouples different spatial grid points and treats them separately, we can easily make predictions for partial saddle points at other resolutions as well. As a proof of concept, we generate a quenched saddle point density profile with a spatial resolution of 2048 at $\chi N = 30$ and $f = 0.40$ using large-cell AF SCFT simulation where we allow the cell length to vary to obtain a stress-free configuration at $L = 205.19 R_g$ (i.e., variable-cell approach[2]). We then apply a single-mode reciprocal space perturbation to obtain a non-saddle point density profile $\phi(\mathbf{r})$, as shown in Fig. 8. The resulting non-saddle point density profile is then used as the target profile in DE-AF simulations, with two types of initializations: one from the ML model prediction, and the other from the solution of the partial saddle point for the corresponding density profiles before perturbation. The latter mimics the standard DE-AF protocol, where the auxiliary field configuration from the previous outer-loop iteration is reused as the initial guess. A field error tolerance of 10^{-5} was applied for these DE-AF simulations. The ML predicted partial saddle points for the $iw_A^*(\mathbf{r})$ and $iw_B^*(\mathbf{r})$ fields appear to be close to the converged ones in simulations, as shown in Fig. 9 (see Sec. S2 of the supplementary material for another example). Consequently, we observe a 3.4× improvement in convergence speed when the simulations are initialized with the ML predictions compared to the aforementioned other initialization. This demonstrates the utility of the model in accelerating simulations beyond the conditions of the data it is trained on.

C. Generalization to higher spatial dimension

Since the local density representation in our ML model is universal across spatial dimensions, we can easily extend our model to higher spatial dimensions. As a proof of concept, we generate new 3D simulation data to fine-tune our model for application in 3D. Specifically, we randomly pick 40 combinations of f and χN in the ranges of $25 \leq \chi N \leq 40$ and $0.22 \leq f \leq 0.35$, and run AF SCFT simulations to obtain the corresponding stress-free saddle-point density profiles of BCC phases with a spatial resolution of $64 \times 64 \times 64$ using the variable-cell approach[2]. We then perturb the BCC phases using the aforementioned single-mode reciprocal space perturbation (with a small $\delta = 0.1$ and $\gamma \sim U[0.90, 1.0]$, similar to the setting in 1D) to obtain non-saddle-point configurations, and run DE-AF simulations to find the corresponding partial saddle points of the auxiliary fields. A field error tolerance of 10^{-5} was applied for these DE-AF simulations. From each configuration we randomly sample 2000 grid points, and partition the sampled data from these 40 configurations of perturbed BCC phases into a training set of 32 configurations and a validation set of 8 configurations, and utilize these new training and validation sets to fine-tune our ML model pre-trained on 1D data. The best model was recorded that yields the lowest loss on the cross validation set after the first 100 epochs during fine-tuning. As shown in Fig. 10, both the training and validation losses decrease rapidly to values below 0.03 within a few hundred epochs, demonstrating the strong generalizability of our ML model. We further test our fine-tuned model by predicting the partial saddle point for a perturbed BCC phase at $\chi N = 29.65$, $f = 0.28$ and $L = 5.57 R_g$ that is generated by the aforementioned single-mode reciprocal space perturbation, and not present in our training and validation sets. As shown in Fig. 11, the ML prediction is in excellent agreement with the simulation results (see Sec. S3 of the supplementary material for another example). Moreover, a simulation initialized from the ML prediction achieves a 3.5×

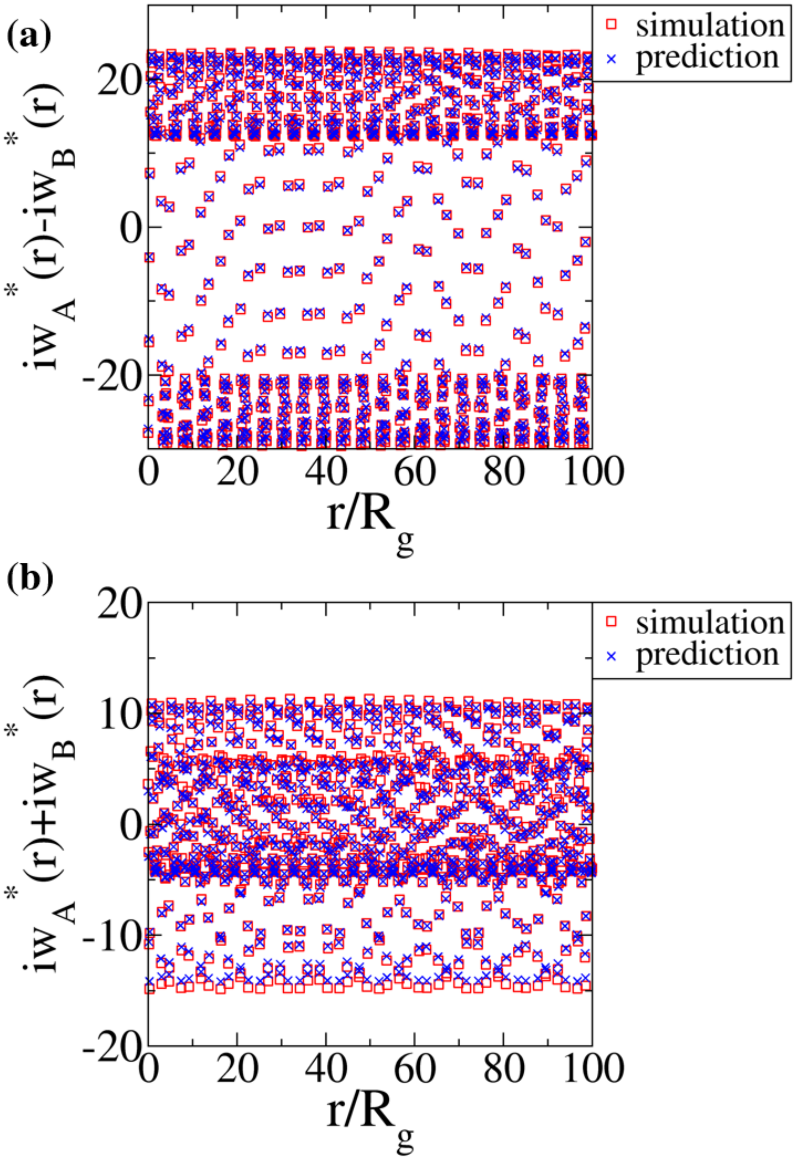

FIG. 9. The partial saddle points $w_A^*(\mathbf{r}) - w_B^*(\mathbf{r})$ (a) and $w_A^*(\mathbf{r}) + w_B^*(\mathbf{r})$ (b) predicted by the ML model (blue) and from simulations (red) for the non-saddle point density profile in Fig. 8 at $\chi N = 30$, $f = 0.40$, and $205.19R_g$. Here we only show a portion of the boxes for better visual clarity.

acceleration in convergence compared to one initialized from the partial saddle point of the corresponding unperturbed BCC phase (which mimics the setting used in a typical DE-AF simulation, as mentioned above). We show that with just a small amount of new data, our trained model can be fine-tuned to perform well in new tasks. This highlights the potential for our ML modeling

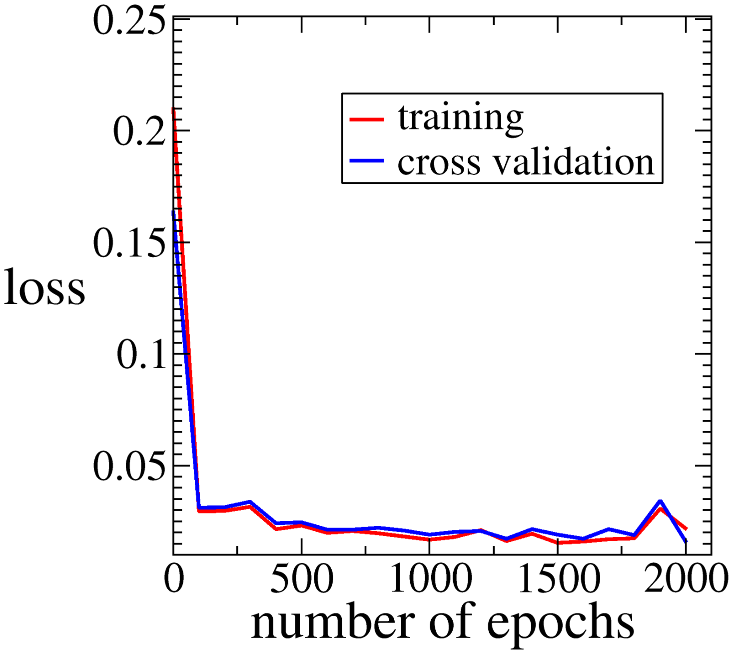

FIG. 10. Training and cross validation loss as functions of the number of epochs for the neural network during fine-tuning using 3D simulation data. The neural network was pre-trained on 1D simulation data as shown in Fig. 6.

scheme to serve as a building block for future models with superior predictive capabilities.

VI. CONCLUSIONS AND DISCUSSION

In this work, we analytically and numerically investigated the partial saddle points of the auxiliary fields corresponding to various density profiles—both those that are saddle points of H and those that are not—in the DE-AF framework of polymer field theory, using a linear diblock copolymer system as an example, and examined factors that affect the solutions of these partial saddle points. This initial study motivated the development of a ML model utilizing an efficient local density feature representation that is applicable across different spatial dimensions and resolutions, and invariant under translations and rotations of the polymer species density fields. We integrated this representation into deep neural networks and trained the models on 1D simulation data with a

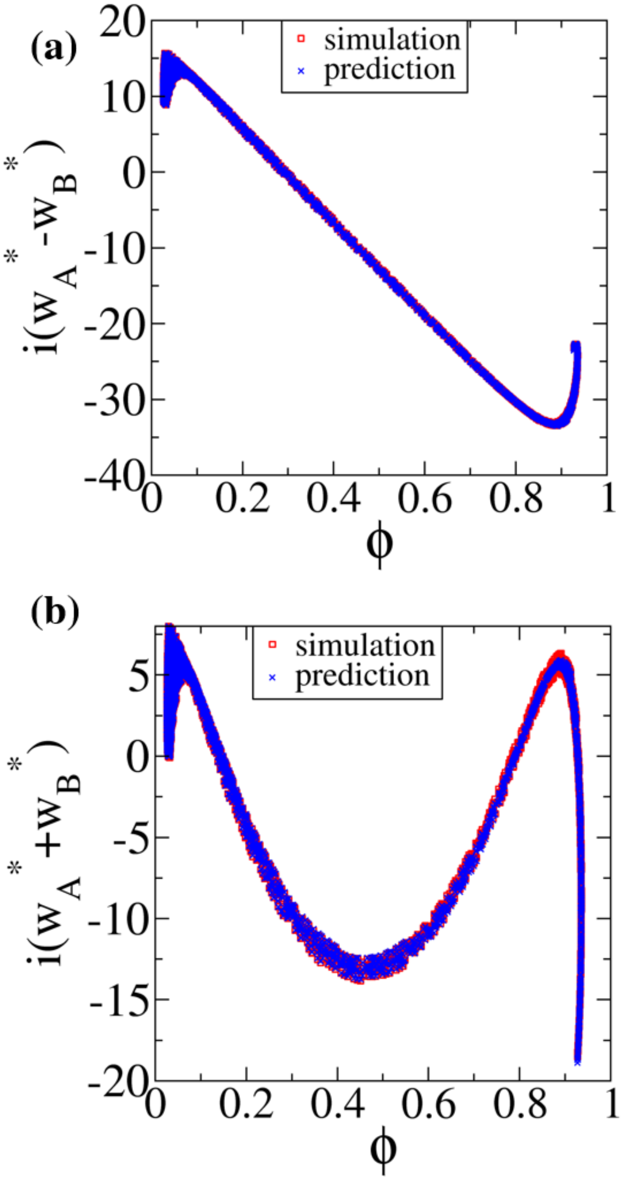

FIG. 11. Machine learned prediction (blue) of the partial saddle points of $w_A^*[\phi] - w_B^*[\phi]$ (a) and $w_A^*[\phi] + w_B^*[\phi]$ (b) along with the corresponding converged solutions from simulation (red) for a perturbed BCC phase at $\chi N = 29.65$, $f = 0.28$ and $L = 5.57R_g$.

spatial resolution of 64 to accurately predict the partial saddle points of the auxiliary fields under varying conditions. Remarkably, the machine-learned model produces high-quality initial guesses that considerably accelerated new simulations—even at resolutions as high as 2048, far exceeding the resolution of the training data. The model was also seen to make excellent prediction of partial saddle points for 3D perturbed BCC structures after fine-tuning with a small amount of 3D data and accelerate new FTS simulations in 3D. Overall, our ML framework could form the basis for new ML-assisted field simulation tools enabling the computational study of various polymer and other soft-matter systems, including multi-species/multi-component systems.

It is noteworthy that our trained ML models can be easily incorporated into existing field simulation tools since they only involve matrix multiplications and simple nonlinear transformations, and the parameters such as the weights W and biases b in the neural networks can be input into the simulation tools just like initial field configurations. Strictly speaking, the ML model accelerates only the solution of partial saddle points of the auxiliary fields at fixed density profiles, which is the inner loop in the DE-AF framework. Although the outer loop that evolves the density profiles remains the same, the overall DE-AF field theory simulation is accelerated.

In addition, we note that here we are invoking the partial saddle point approximation, and given a density profile the algorithm seeks one scalar auxiliary field for each species in the system. Therefore, when making predictions for the partial saddle points, we can employ standard feed-forward deep neural networks, which are relatively simple deep ML models. Alternatively, if one wants to accelerate fully fluctuating, density-explicit field-theoretic simulations (FTS), where in the inner loop one is sampling a *distribution* of field configurations for each species auxiliary field, there are more advanced deep learning models such as diffusion models[31] that are well suited for such a task.

SUPPLEMENTARY MATERIAL

The supplementary material provides additional examples that further demonstrate the performance of our machine learning models.

ACKNOWLEDGMENTS

This work was supported by the U.S. Department of Energy, Office of Basic Energy Sciences, under Award Number DE-SC0019001. H. D. C. acknowledges partial support by the National Science Foundation under Award Number DMS-2410252. Use was made of computational facilities purchased with funds from the National Science Foundation (OAC-1925717 and CNS-1725797) and administered by the Center for Scientific Computing (CSC). The CSC is supported by the California NanoSystems Institute and the Materials Research Science and Engineering Center (MRSEC; NSF DMR-2308708) at UC Santa Barbara. The research reported here made use of shared facilities of the UC Santa Barbara MRSEC (NSF DMR-2308708), a member of the Materials Research Facilities Network (www.mrfn.org) and the BioPACIFIC Materials Innovation Platform of the National Science Foundation under Award No. DMR-1933487.

REFERENCES

[1] G. H. Fredrickson, V. Ganesan, and F. Drolet, "Field-theoretic computer simulation methods for polymers and complex fluids," Macromolecules **35**, 16–39 (2002).

[2] G. H. Fredrickson, *The equilibrium theory of inhomogeneous polymers*, 134 (Oxford University Press: Oxford, 2006).

[3] K. T. Delaney and G. H. Fredrickson, "Recent developments in fully fluctuating field-theoretic simulations of polymer melts and solutions," J. Phys. Chem. B **120**, 7615–7634 (2016).

[4] M. W. Matsen, "Field theoretic approach for block polymer melts: SCFT and FTS," J. Chem. Phys. **152** (2020).

[5] S. F. Edwards, "The statistical mechanics of polymers with excluded volume," Proc. Phys. Soc. **85**, 613 (1965).

[6] G. H. Fredrickson and K. T. Delaney, *Field Theoretic Simulations in Soft Matter and Quantum Fluids*, Vol. 173 (Oxford University Press, 2023).

[7] J. Hubbard, "Calculation of partition functions," Phys. Rev. Lett. **3**, 77 (1959).

[8] A. Weyman, V. G. Mavrantzas, and H. C. Öttinger, "Field-theoretic simulations beyond δ-interactions: Overcoming the inverse potential problem in auxiliary field models," J. Chem. Phys. **155** (2021).

[9] A. Weyman, V. G. Mavrantzas, and H. C. Öttinger, "Direct calculation of the functional inverse of realistic interatomic potentials in field-theoretic simulations," J. Chem. Phys. **156** (2022).

[10] T. Quah, K. T. Delaney, and G. H. Fredrickson, "Preserving positivity in density-explicit field-theoretic simulations," J. Chem. Phys. **161** (2024).

[11] M. Müller and F. Schmid, "Incorporating fluctuations and dynamics in self-consistent field theories for polymer blends," Advanced Computer Simulation Approaches for Soft Matter Sciences II , 1–58 (2005).

[12] J. G. E. M. Fraaije, "Dynamic density functional theory for microphase separation kinetics of block copolymer melts," J. Chem. Phys. **99**, 9202–9212 (1993).

[13] J. G. E. M. Fraaije, B. A. C. Van Vlimmeren, N. M. Maurits, M. Postma, O. A. Evers, C. Hoffmann, P. Altevogt, and G. Goldbeck-Wood, "The dynamic mean-field density functional method and its application to the mesoscopic dynamics of quenched block copolymer melts," J. Chem. Phys. **106**, 4260–4269 (1997).

[14] C. Yeung and A.-C. Shi, "Formation of interfaces in incompatible polymer blends: A dynamical mean field study," Macromolecules **32**, 3637–3642 (1999).

[15] R. Hasegawa and M. Doi, "Adsorption dynamics. extension of self-consistent field theory to dynamical problems," Macromolecules **30**, 3086–3089 (1997).

[16] T. Quah, C. Balzer, K. T. Delaney, and G. H. Fredrickson, "Efficient dynamical field-theoretic simulations for multi-component systems," J. Chem. Phys. **162** (2025).

[17] Y. Xuan, K. T. Delaney, H. D. Ceniceros, and G. H. Fredrickson, "Deep learning and self-consistent field theory: A path towards accelerating polymer phase discovery," J. Comput. Phys. **443**, 110519 (2021).

[18] Y. Xuan, K. T. Delaney, H. D. Ceniceros, and G. H. Fredrickson, "Machine learning and polymer self-consistent field theory in two spatial dimensions," J. Chem. Phys. **158** (2023).

[19] P. Chen and K. D. Dorfman, "Gaming self-consistent field theory: Generative block polymer phase discovery," Proc. Natl. Acad. Sci. U.S.A. **120**, e2308698120 (2023).

[20] I. Nakamura, "Phase diagrams of polymer-containing liquid mixtures with a theory-embedded neural network," New J. Phys. **22**, 015001 (2020).

[21] Q. Wei, Y. Jiang, and J. Z. Y. Chen, "Machine-learning solver for modified diffusion equations," Phys. Rev. E **98**, 053304 (2018).

[22] D. Lin and H.-Y. Yu, "Deep learning and inverse discovery of polymer self-consistent field theory inspired by physics-informed neural networks," Phys. Rev. E **106**, 014503 (2022).

[23] S. Zhao, T. Cai, L. Zhang, W. Li, and J. Lin, "Autonomous construction of phase diagrams of block copolymers by theory-assisted active machine learning," ACS Macro Lett. **10**, 598–602 (2021).

[24] D. Yong and J. U. Kim, "Accelerating langevin field-theoretic simulation of polymers with deep learning," Macromolecules **55**, 6505–6515 (2022).

[25] M. Zhao and W. Li, "Laves phases formed in the binary blend of ab4 miktoarm star copolymer and a-homopolymer," Macromolecules **52**, 1832–1842 (2019).

[26] W. Kang, D. Yong, and J. U. Kim, "Characteristics of the complex saddle point of polymer field theory," Macromolecules **57**, 3850–3861 (2024).

[27] L. Zhang, J. Han, H. Wang, R. Car, and W. E, "Deep potential molecular dynamics: a scalable model with the accuracy of quantum mechanics," Phys. Rev. Lett. **120**, 143001 (2018).

[28] J. Zeng, D. Zhang, D. Lu, P. Mo, Z. Li, Y. Chen, M. Rynik, L. Huang, Z. Li, S. Shi, *et al.*, "Deepmd-kit v2: A software package for deep potential models," J. Chem. Phys. **159** (2023).

[29] J. T. Barron, "Continuously differentiable exponential linear units," arXiv preprint arXiv:1704.07483 (2017).

[30] D. P. Kingma, "Adam: A method for stochastic optimization," arXiv preprint arXiv:1412.6980 (2014).

[31] D. E. Habibi, G. Aarts, L. Wang, and K. Zhou, "Diffusion models learn distributions generated by complex langevin dynamics," arXiv preprint arXiv:2412.01919 (2024).